

Infrared driven CO oxidation reactions on isolated platinum cluster oxides, Pt_nO_m^+

Alexander C. Hermes,^a Suzanne M. Hamilton,^a Graham A. Cooper,^a
Christian Kerpel,^b Dan J. Harding,^b Gerard Meijer,^b André
Fielicke^{b*} and Stuart R. Mackenzie^{a*}

DOI: 10.1039/b000000x [DO NOT ALTER/DELETE THIS TEXT]

This collaboration has recently shown that infrared excitation can drive decomposition reactions of molecules on the surface of gas-phase transition metal clusters. We describe here a significant extension of this work to the study of bimolecular reactions initiated in a similar manner. Specifically, we have observed the infrared activated CO oxidation reaction ($\text{CO}_{(\text{ads})} + \text{O}_{(\text{ads})} \rightarrow \text{CO}_{2(\text{g})}$) on isolated platinum oxide cations, Pt_nO_m^+ . Small platinum cluster oxides Pt_nO_m^+ ($n = 3-7$, $m = 2,4$), have been decorated with CO molecules and subjected to multiple photon infrared excitation in the range 400–2200 cm^{-1} using the Free Electron Laser for Infrared eXperiments (FELIX). The $\text{Pt}_n\text{O}_m\text{CO}^+$ clusters have been characterised by infrared multiple photon dissociation spectroscopy using messenger atom tagging. Evidence is observed for isomers involving both dissociatively and molecularly adsorbed oxygen on the cluster surface. Further information is obtained on the evolution of the cluster structure with number of platinum atoms and CO coverage. In separate experiments, $\text{Pt}_n\text{O}_m\text{CO}^+$ clusters have been subjected to infrared heating via the CO stretch around 2100 cm^{-1} . On all clusters investigated, the CO oxidation reaction, indicated by CO_2 loss and production of $\text{Pt}_n\text{O}_{m-1}^+$, is found to compete effectively with the CO desorption channel. The experimental observations are compared with the results of preliminary DFT calculations in order to identify both cluster structures and plausible mechanisms for the surface reaction.

30

^a Department of Chemistry, University of Oxford, Physical and Theoretical Chemistry Laboratory, South Parks Road, Oxford, OX1 3QZ, U.K. Fax: 44 (0)1865 275410; Tel: 44 (0)1865 275156; E-mail: stuart.mackenzie@chem.ox.ac.uk

35

^b Fritz-Haber-Institut der Max-Planck-Gesellschaft, Faradayweg 4-6, D-14195 Berlin, Germany. Fax: 49 (0)30 8413 5603; Tel: 49 (0)30 8413 5622; E-mail: fielicke@fhi-berlin.mpg.de

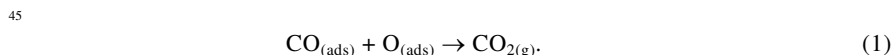
1 Introduction

One of the major driving forces behind research into isolated metal clusters is the prospect of developing a better understanding of the chemistry of defect sites which play a key role in practical heterogeneous catalysis.^{1, 2} Very small clusters (less than 5 10 metal atoms) with no long-range order can have a variety of different coordination sites and, in many respects, represent experimentally and computationally tractable model catalytic systems.³⁻⁵ To this end the full range of modern gas-phase spectroscopic and mass spectrometric techniques have been brought to bear on a central aim in cluster science – understanding the evolution of 10 electronic and geometrical structure with cluster size. Reflecting their central role in catalysis, much of this effort has been directed at clusters of transition metal atoms. Our understanding of these systems has improved enormously over recent years with experiments finally providing reliable spectroscopic data against which to benchmark computational studies.

One major advance in the spectroscopy of small clusters has been the recent emergence of infrared multiple photon dissociation (IR-MPD) spectroscopy as a powerful method for investigating the vibrational structures of isolated metal clusters. The use of inert messenger tagging,^{6, 7} in which absorption of IR photons is registered by the concomitant loss of, for example, a physisorbed rare-gas atom, has 20 extended the range of the method beyond cluster adsorbate systems⁸ to naked metal clusters.⁹⁻¹² These action spectroscopy techniques couple the sensitivity of mass spectrometric detection with the high fluence and wide wavelength tunability of modern laser sources and thus permit the study of isolated clusters in molecular beams or ion traps.

We have recently demonstrated that, in addition to driving the desorption of weakly-bound species, direct infrared pumping may be used to trigger interesting chemistry on isolated clusters in a manner similar to temperature programmed reaction on extended surfaces.^{13, 14} IR excitation of nitrous oxide molecularly bound on cationic rhodium clusters was shown to cause efficient decomposition of the N₂O 30 moiety resulting in the generation of rhodium oxide clusters and the loss of molecular nitrogen. All indications are that the reaction is thermal with the same processes occurring with similar efficiency following pumping of the Rh-O mode in Rh_nON₂O⁺. These studies yield a wealth of valuable and unique information on desorption and reaction barriers as a function of cluster size and structure. This was 35 exemplified recently when we demonstrated that the marked difference in the efficiency of the surface reaction on Rh₅N₂O⁺ and Rh₅ON₂O⁺ clusters arises as a result of subtle variations in the barrier heights for reaction and N₂O desorption between the two.¹⁵ A second example is the size-dependence of the IR-induced dehydrogenation of methane initially molecularly bound to cationic platinum 40 clusters.¹⁶ These experiments are only possible using an isotopically enriched Pt sample, which has also been used in the studies described in the following.

Here, we report a significant extension of this infrared driven cluster surface reactivity to the study of bimolecular reactions. Specifically, we have studied the CO oxidation reaction on platinum cluster oxides which can be summarised as



CO-oxidation over transition metal catalysts is one of the best studied reactions of its type.¹⁷ It is believed to proceed *via* a classic Langmuir-Hinshelwood mechanism following adsorption of CO and dissociative adsorption of O₂ to the catalytic surface. Temperature programmed reaction studies on Pt(111) as well as polycrystalline platinum surfaces indicate at least two CO₂ formation mechanisms on extended surfaces. α -CO₂, produced around 160 K, results from the reaction of hot oxygen atoms produced upon O₂ dissociation and thus depends critically on the presence of co-adsorbed O₂ molecules. By contrast β -CO₂, whose production exhibits a pronounced maximum at 260 K, results from reaction of CO with co-adsorbed oxygen *adatoms* and is thus highly sensitive to the local environment.¹⁸ The ratio of the two components is strongly dependent on both the O₂ and CO coverage.

In pioneering studies of their type, reaction (1) has been studied by Heiz *et al.* on monodisperse platinum clusters deposited on MgO(100) films in the size regime Pt_{*n*} (*n* ≤ 20).¹⁹ Strong variations in the number of CO₂ molecules produced per platinum atom were observed as a function of cluster size. In particular, step increases in efficiency around *n*=8 and *n*=15 were interpreted as resulting from the change from pseudo two to three-dimensional structures.

On isolated, gas-phase clusters, Shi and Ervin, were the first to establish a full catalytic cycle involving the oxidation of CO on Pt_{*n*}⁻ (*n* = 2–6) anionic clusters under thermal conditions.²⁰ Using guided ion beam techniques, Pt_{*n*}⁻ clusters were oxidised by collision with O₂ or N₂O to produce Pt_{*n*}O_{*m*}⁻ and subsequently reacted with CO to regenerate the original clusters. The same N₂O/CO scheme was used by Balaj *et al.* in Fourier transform ion cyclotron resonance (ICR) experiments to study reactions of cationic clusters, Pt_{*n*}⁺ (*n* = 6–8).²¹ The long storage times in the ICR experiments permitted the establishment of steady state conditions which were poisoned by a high surface CO coverage.

Our approach represents something of a hybrid method for studying reactions on clusters. First we decorate isolated clusters with reactive precursors (O₂ and CO) under thermal conditions (~300 K), allowing the stabilisation of intermediate species not usually observed under single collision reaction conditions. Then, *via* IR pumping of an allowed vibrational transition, we raise the internal energy of the cluster complex to initiate surface processes such as desorption, reaction-desorption, *etc.*. Simultaneous mass spectrometric monitoring of all mass channels permits depletions in one channel to be matched with enhancements in others providing a detailed picture of any reactive dynamics resulting in moiety loss from the cluster.

2 Experimental

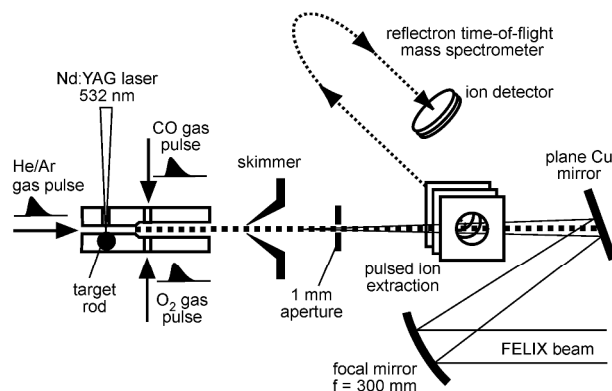


Fig.1 Scheme of the experiment used for IR multiple photon dissociation of metal-cluster rare-gas complexes.

All experiments were carried out at the Free Electron Laser for Infrared eXperiments (FELIX)²² facility in the Netherlands. The basic experimental setup has been described previously in detail^{10, 23} and is shown schematically in Figure 1. The essential features are as follows. $^{194}\text{Pt}_n^+$ cluster cations are generated via 532 nm pulsed laser ablation of an isotopically enriched ^{194}Pt foil wrapped around a target rod. The ablation products are entrained within a short, intense (8 bar backing pressure) pulse of helium gas seeded with argon (~1%). Cooling and clustering occurs as the gas pulse travels down a narrow channel held at ambient temperature.

In a development from previous experiments, two pulsed valves allow controlled injection of molecular oxygen, O_2 (typical backing pressure 500 mbar), and/or carbon monoxide, CO (1.2 bar), respectively, into the reaction channel. These gases can react with the newly formed clusters generating a range of new $\text{Pt}_n\text{O}_m\text{CO}^+$ species allowing the user a degree of control over the product distribution *via* the partial pressures of the respective reactants. This approach was found to provide more flexibility than could be obtained with a single valve and premixed O_2/CO .

After exiting the cluster channel, the molecular beam passes through a 2 mm diameter skimmer and a 1 mm diameter aperture into the extraction region of a reflectron time-of-flight mass spectrometer. Here it is met by the counter-propagating IR beam delivered by FELIX (*ca.* 20 mJ/pulse) which is loosely focused onto the aperture and synchronized with the molecular beam ensuring good spatial and temporal overlap of the IR and cluster beams.

Mass spectra are collected at a rate of 10 Hz with the FELIX beam enabled on alternate shots to collect ‘on’ and ‘off’ spectra. From these, a difference mass spectrum is obtained at each wavelength. This difference, as a function of wavelength, yields the IR-MPD spectrum for each point in the mass spectrum. Depletion of a parent ion peak is indicative of a resonant loss process, whose nature can be determined by looking for concomitant enhancements in product species.

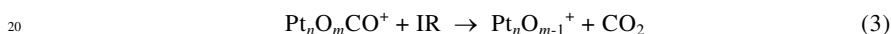
Similarly, the relative cross sections can be calculated from the relative depletion and normalization by the photon fluence.

All IR spectra are recorded at 5 cm⁻¹ intervals and several scans are averaged to increase the spectral signal to noise ratio. The IR-MPD spectra cover the range 400–
5 2200 cm⁻¹ encompassing both metal oxide (Pt-O) vibrations as well as the CO stretching region. The reactivity studies concentrated primarily on processes induced following absorption in the CO stretch region around 2100 cm⁻¹.

Two conceptually different experiments are performed: Firstly, conventional IR-MPD spectra of Ar-tagged clusters, in tandem with quantum-chemical spectral
10 simulations, provide important information on the cluster structures. In this case, whenever IR radiation is absorbed by the cluster, rapid intramolecular redistribution of energy leads to heating of the cluster and the subsequent desorption of the physisorbed Ar atom:



Secondly, infrared pumping is used to heat the clusters in order to trigger chemical reactivity between moieties co-adsorbed on the cluster surface:



In these experiments, there is deliberately no mass selection in the cluster source. This permits the spectra of all species generated in the beam to be recorded simultaneously. However, it does present potential problems in identifying
25 unambiguously enhancements in one channel with depletions elsewhere. To this end, in order to maximise our chances of observing IR-induced CO oxidation reactions, O₂ was used as the source of oxygen atoms. In this way complexes with *even* numbers of O atoms *i.e.*, Pt_nO_m⁺ (*m* = 2, 4, ...) and Pt_nO_mCO⁺ (*m* = 2, 4, ...) are generated preferentially. The products of any CO oxidation reaction (3) are
30 consequently observed as enhancements in the *odd* (*i.e.*, *m*-1) oxide mass channels against a nominally zero background.

3 Computational

In support of the experiments described above we have undertaken a computational study of low-lying $\text{Pt}_n\text{O}_2\text{CO}^+$ ($n = 3-5$) structures and plausible CO oxidation pathways on these clusters.

All calculations were carried out using Density Functional Theory (DFT) as implemented in the Turbomole 6.0 package.²⁴ In common with our previous findings, no single exchange-correlation functional provides the best performance for every type of calculation that is required.¹⁴ However, the TPSS functional^{25, 26} has previously yielded good agreement with experiments of this type²⁷ (including Pt_n^+ spectra)²⁸ and provides a good compromise in performance for each type of calculation. In our previous work with high-spin rhodium clusters, we used the hybrid variant of this functional (TPSSh).²⁶ However, in the current work, in which low spin states dominate, we find both functionals favour the same low-energy structures, including the putative global minimum, with only small differences in the relative energies. As a result, for the current study, the TPSS functional has been used throughout. Triple- ζ valence basis sets (def2-TZVP)^{29, 30} were used for all atoms, with def2-ecp effective core potentials representing the core electrons of the platinum atoms.

Initial structures for the clusters were derived as follows: A range of Pt_nO_2^+ structures was generated via a combination of DFT-based basin hopping³¹ and by addition of O_2 to the experimentally determined Pt_n^+ structures. CO was then added to these structures in a variety of likely binding geometries to provide the starting points of the calculations. A range of spin states were explored for each cluster and normal mode analyses confirmed the identity of minima or transition states as well as providing the spectral simulations. In all of the low-lying geometries calculated, the doublet spin state ($2S+1=2$) is predicted to lie significantly lower in energy than higher spin states. As a result, all of the computational data presented henceforth refer to the doublet unless stated otherwise. Spin-orbit coupling was not included in the calculations here. The results of previous computational studies which have include spin-orbit coupling are inconclusive with several reporting no effect on the relative isomer ordering.³²

For ease of comparison with the experimental data, the calculated stick spectra are broadened with a Gaussian line shape (18 cm^{-1} line width).

4 Results and Discussion

4.1 IR-MPD Spectroscopy of $\text{Pt}_n\text{O}_m\text{CO}^+$

A typical mass spectrum recorded in the region of the Pt_4^+ cluster is shown in Figure 2 illustrating the range of complexes produced in the source. The dominant species present, as designed, are complexes with a single CO and/or O_2 molecule (note that the mass spectrum yields no conclusive information regarding the molecular / dissociative nature of the adsorption). Although there is evidence of monoxide clusters, these have low intensity compared with the even oxides. All intense peaks in the mass spectrum have an Ar-tagged counterpart 40 u higher in mass resulting from the 1% Ar used in the carrier gas. These are used for the IR-MPD spectra in order to gain structural information. Interestingly, secondary clustering (with O_2 , CO) was observed to be significantly less efficient without the presence of the Ar suggesting that it plays a role in the clustering process itself.

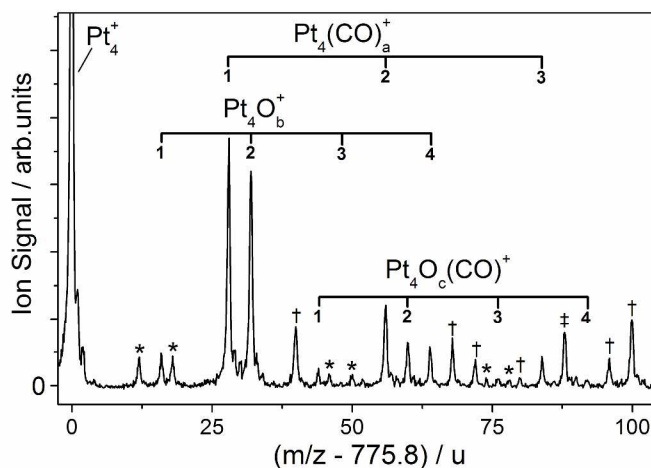


Fig. 2 Time-of-flight mass spectrum recorded in the region of Pt_4^+ complexes in the absence of IR radiation. (*) Minor Pt_4X^+ species ($\text{X}=\text{N}$, H_2O , *etc.*). (†) Ar tagged species. (‡) $\text{Pt}_4\text{O}_2(\text{CO})_2$. The spectrum is dominated by species with even numbers of oxygen atoms as expected when using molecular O_2 as the oxygen source.

Figure 3 a) shows the full IR-MPD spectrum of the $\text{Pt}_4\text{O}_2\text{COAr}^+$ cluster from 400–2200 cm^{-1} . This region encompasses the fundamental vibrational transitions from Pt–O stretches / bends (400–700 cm^{-1}) to the CO stretch (2125 cm^{-1}) and a number of strong, well-resolved, bands are observed. Aid in the assignment of the spectrum comes from the simulated spectra provided by the DFT calculations. The simulated IR spectrum for the lowest energy structure obtained (the putative global minimum) is shown in Figure 3 b). This is a buckled two dimensional Pt_4 structure with the CO bound atop and with the oxygen dissociatively adsorbed in bridge sites. The calculated spectrum shows excellent agreement with the experimental spectrum below 750 cm^{-1} and the CO stretching band observed at 2125 cm^{-1} is similarly well-reproduced.

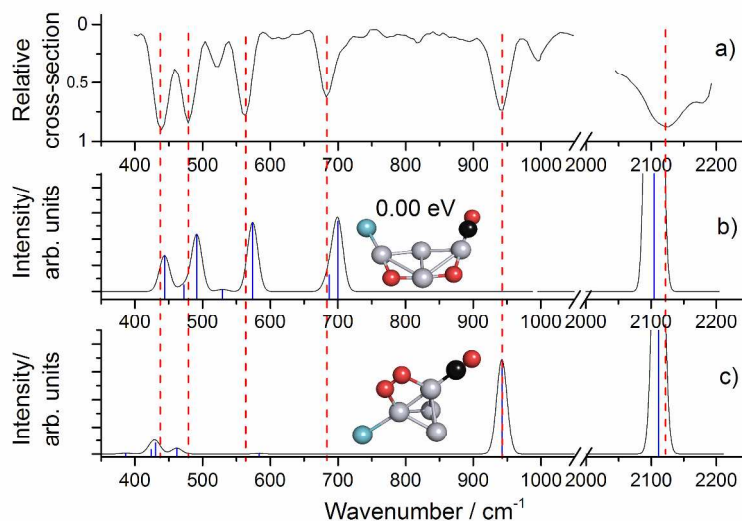


Fig. 3 a) Experimental IR-MPD spectrum of $\text{Pt}_4\text{O}_2\text{COAr}^+$ (note the spectrum is shown inverted, *i.e.*, cross section increasing down to reflect the fact that this spectrum is recorded by observing the depletion of $\text{Pt}_4\text{O}_2\text{COAr}^+$). b) Calculated spectrum (TPSS/def2-TZVP) of the calculated lowest lying isomer identified. c) Calculated spectrum of a low-lying peroxo-type isomer (the Ar tagged structure 12, see ESI).

One important spectral feature (*ca.* 940 cm^{-1}) cannot, however, be explained by the lowest energy calculated structure. On the basis of comparison with simulated spectra of calculated structures two possible carriers for this band have been identified. One involves isomers with atop bound oxygen atoms. These typically lie $>1\text{ eV}$ above the putative global minimum structure and have calculated Pt-O stretches up to 900 cm^{-1} . They also have additional features in the low frequency range ($400\text{--}600\text{ cm}^{-1}$) for which, however, there is little evidence in the experimental spectrum. An intriguing alternative, whose agreement with the experimental spectrum is marginally better, is the presence of peroxo-type isomers of which one example is shown in Figure 3 c). The structure shown in Figure 3 c) has been selected for its match with the experimental band but is not the lowest energy peroxo-structure calculated (see ESI). Given the potential need to scale the calculated frequencies, as well as possible spectral shifts introduced by the presence of co-adsorbed Ar atoms, it is impossible to assign this single spectral feature to a particular peroxo-structure. All such peroxo-structures, however, are calculated to lie $>1.4\text{ eV}$ above the lowest energy isomer (see SI) and have peroxo bands in the range $900 \pm 50\text{ cm}^{-1}$. It is noteworthy that the spectral position of the peroxo band is unusually sensitive to the exchange correlation functional used in the simulation, appearing, on average, 100 cm^{-1} further to the blue in calculations using TPSSh compared to the TPSS spectrum shown in Figure 3.

On extended platinum surfaces, temperature programmed desorption experiments provide good evidence of both molecular and dissociative binding of O_2 , showing O_2 evolution at between $150\text{--}200\text{ K}$ (molecularly adsorbed) and $> 700\text{ K}$ (dissociatively adsorbed).³³

Whether the band at 940 cm^{-1} is assigned to atop-bound oxygen atoms or peroxo-structures, in order to account for all features in the observed spectrum it is necessary to invoke the presence of multiple isomers within our molecular beam. The possible presence of the peroxo-structures is particularly unexpected given their calculated high energy, especially given the apparent absence of other lower-lying isomeric forms. It is, however, possible that the peroxo-structures become trapped in a deep local minimum during the clustering process, perhaps as a result of boiling off pre-adsorbed Ar atoms. This raises the possibility that the structures of the Ar-tagged clusters are not representative of the same species without the Ar present.

10

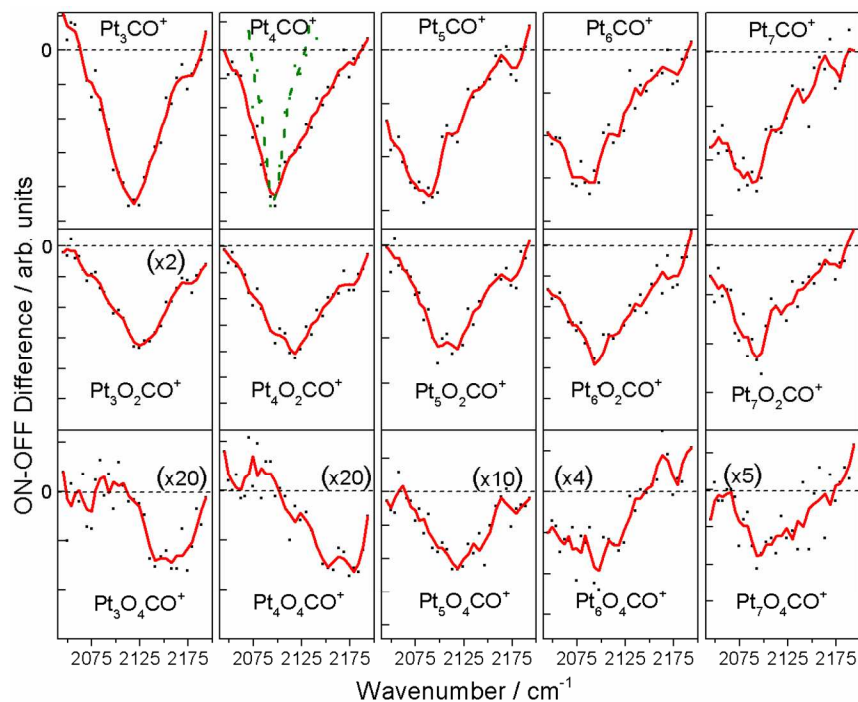


Fig 4 IR-MPD spectra of $\text{Pt}_n\text{O}_m\text{CO}^+$ ($n=3-7$, $m=0, 2, 4$) clusters in the CO stretch region (black dots: raw data, red line: 5 point adjacent average). The green dashed line shows the spectrum recorded for Pt_3CO^+ with 5 dB attenuation of the IR beam illustrating the degree of saturation achieved. Note the slight red shift of the ν_{CO} peak as the number of platinum atoms increases and the blue-shift with increasing oxygen coverage.

Ar-tagging is not necessary in recording IR-MPD spectra in the CO stretching region, with CO loss itself being an effective signature of IR absorption. Figure 4 shows the CO-loss IR-MPD spectrum of $\text{Pt}_n\text{O}_m\text{CO}^+$ clusters recorded in the region $2050-2200\text{ cm}^{-1}$. The observed peak centres deduced from attenuated spectra are presented in Table 1. Two trends are clear; Firstly, for otherwise identical species, there is a small red-shift in the CO stretch, ν_{CO} , with increasing number of platinum atoms, n . This has been observed previously for CO binding on bare clusters by Gruene *et al.*³⁴ and can be understood in terms of a simple back-bonding model of CO chemisorption in which additional electron density increasingly weakens the CO

bond by π -backdonation. By way of comparison, the vibrational frequency of CO atop-bound on extended Pt(111) surfaces is $2095 \pm 10 \text{ cm}^{-1}$.^{35, 36} Secondly, there is a marked blue-shift in ν_{CO} with increasing oxygen coverage (*i.e.*, down Figure 4). This effect is largest on the very smallest clusters. This, too can be understood qualitatively on the basis of back-bonding with oxygen adatoms locally fixing electron density and reducing the scope for π -backdonation to CO. A similar effect was observed for H-atoms co-adsorbed with CO on cobalt cluster cations.³⁷

Table 1 CO stretching band centres for $\text{Pt}_n\text{O}_m\text{CO}^+$ ($n=3-7$, $m=0, 2, 4$) extracted from Gaussian fits of the IR-MPD spectra. Where the signal to noise was acceptable ($n=4-6$) the IR-attenuated data was used otherwise the full power spectra were used. For species common to both studies, these values are in good agreement with those of the earlier study by Gruene *et al.*³⁴

n	m	Peak centre, $\nu_{\text{CO}} / \text{cm}^{-1}$	Band shift $\Delta\nu / \text{cm}^{-1}$
3	0	2120 ± 5^1	0
3	2	2127 ± 8^1	7
3	4	2156 ± 8^1	46
4	0	2097 ± 2.5	0
4	2	2125 ± 2.5	28
4	4	2164 ± 5	67
5	0	2080 ± 2.5	0
5	2	2112 ± 5	32
5	4	2118 ± 5	37
6	0	2078 ± 5	0
6	2	2092 ± 5	14
6	4	2087 ± 10^1	9
7	0	2072 ± 8^1	0
7	2	2090 ± 5^1	18
7	4	2109 ± 10^1	37

¹Full power spectrum used

15

4.2 IR-driven CO oxidation reactions

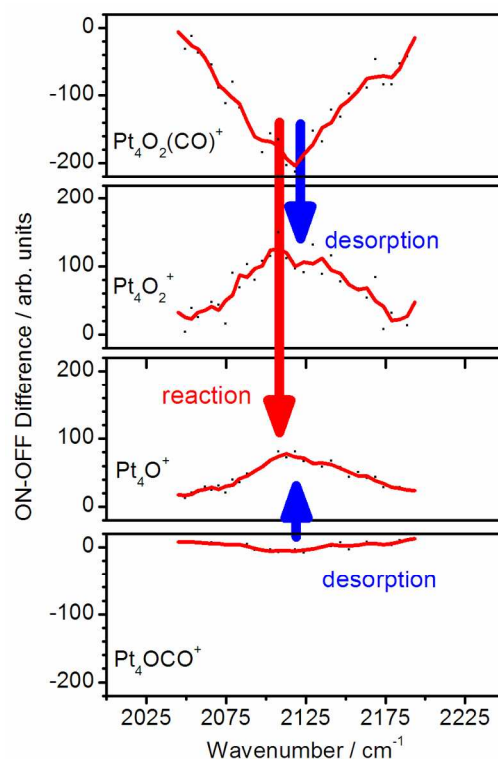
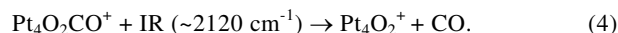


Fig. 5 IR-MPD spectrum of $\text{Pt}_4\text{O}_2\text{CO}^+$ showing a strong signal depletion upon excitation in the region of the CO stretching frequency at 2120 cm^{-1} (black dots: raw data, red line: 5 point adjacent average). Accompanying the above depletion, enhancements are observed at the same spectral position in the Pt_4O_2^+ and Pt_4O^+ mass channels. The depletion in the Pt_4OCO^+ channel (bottom), whilst observed, is much too small to account for the increase in Pt_4O^+ by CO loss.

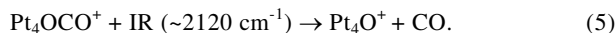
While spectral characterisation is performed using the Ar messenger with attenuated IR intensity as described above, in other experiments the $\text{Pt}_n\text{O}_m\text{CO}^+$ clusters were subjected to intense infrared excitation via the CO stretch in order to initiate surface reaction processes and/or desorption of the CO. The results for a typical cluster, $\text{Pt}_4\text{O}_2\text{CO}^+$, are shown in Figure 5. The top spectrum shows the depletion in the parent ion ($\text{Pt}_4\text{O}_2\text{CO}^+$) signal as a function of excitation wavenumber. This spectrum has been corrected for the component which depletes into this mass channel, *e.g.*, Ar loss from $\text{Pt}_4\text{O}_2\text{COAr}^+$, and CO loss from $\text{Pt}_4\text{O}_2(\text{CO})_z$ ($z \geq 2$). The loss in the parent signal is mirrored by a concomitant increase in the signal observed in a variety of lower mass channels. Perhaps unsurprisingly, the largest of the enhancements observed in the same spectral region is in the Pt_4O_2^+ channel and corresponds to IR-MPD resulting in simple CO loss:

20



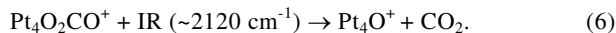
More interestingly from a reactivity perspective, the same spectral feature is also

observed in the Pt_4O^+ mass channel. In principle, this signal could arise from CO loss from the monoxide cluster,



However, as the intensity difference spectrum at the bottom of Figure 5 shows, the depletion in the Pt_4OCO^+ channel is much too small to account for the increase in the Pt_4O^+ signal observed. Indeed, the observed Pt_4O^+ enhancement is larger than the total Pt_4OCO^+ signal (see Figure 2) due to the use of O_2 in the production of the clusters.

Instead, the Pt_4O^+ signal is interpreted as the signature of cluster surface reactivity induced by infrared heating of the parent $\text{Pt}_4\text{O}_2\text{CO}^+$ cluster complex, in this case CO oxidation generating CO_2 :



This is an important finding, as it indicates that infrared driven cluster chemistry is more general than the surface decomposition we have studied previously.^{13, 14}

In these experiments, it is possible to quantify the change in signal intensity (*i.e.*, the depletions and enhancements) in each channel and, within mutual experimental uncertainties, the sum of the Pt_4O_2^+ and Pt_4O^+ enhancements is equal to the total depletion observed in the parent ion channel. This indicates that CO loss and the $\text{CO} + \text{O} \rightarrow \text{CO}_2$ reaction are the only significant processes which result in parent ion signal loss.

Similar CO oxidation reactions are observed on all platinum cluster sizes studied here (*i.e.*, $\text{Pt}_n\text{O}_2\text{CO}^+$, $n = 3-7$) as shown in Figure 6. By comparing (integrated) intensity differences in the different product channels across the spectral region explored it is possible to extract representative branching ratios for the reaction *vs* CO desorption channels and these are shown in Table 2. These branching ratios show little size dependence in the cluster range studied here with the reactive channel accounting for approximately 35 – 45% of the parent signal loss. It would appear that there are no inert clusters in this size range, nor any with anomalously high reactivity. It is difficult to compare these numbers directly with the kinetic studies on isolated clusters such as those of Shi *et al.*²⁰ and Balaj *et al.*²¹ as mass spectrometric collision experiments are, by their nature, insensitive to ineffective collisions (*e.g.*, $\text{CO} + \text{Pt}_n^+ \rightarrow \text{Pt}_n^+ + \text{CO}$). However, Balaj *et al.* noted that, unlike $n = 6-8$, Pt_5^+ failed to establish an efficient catalytic cycle due to CO binding unreactively to the oxide and dioxide clusters.

The experimental data regarding the CO oxidation reaction following pumping of the peroxo band at 940 cm^{-1} are inconclusive. Any depletion in the $\text{Pt}_4\text{O}_2\text{CO}^+$ signal that is observed in this spectral region is, unfortunately, obscured by a larger depletion into this mass channel by Ar loss from $\text{Pt}_4\text{O}_2\text{COAr}^+$ (see Figure 3). In addition, there is no evidence of enhancement in this region in the Pt_4O^+ channel which would signify CO_2 loss. The spectrum in the CO loss channel is further obscured by the fact that Pt_4O_2^+ and its Ar- tagged variant have strong absorptions of their own in this region.

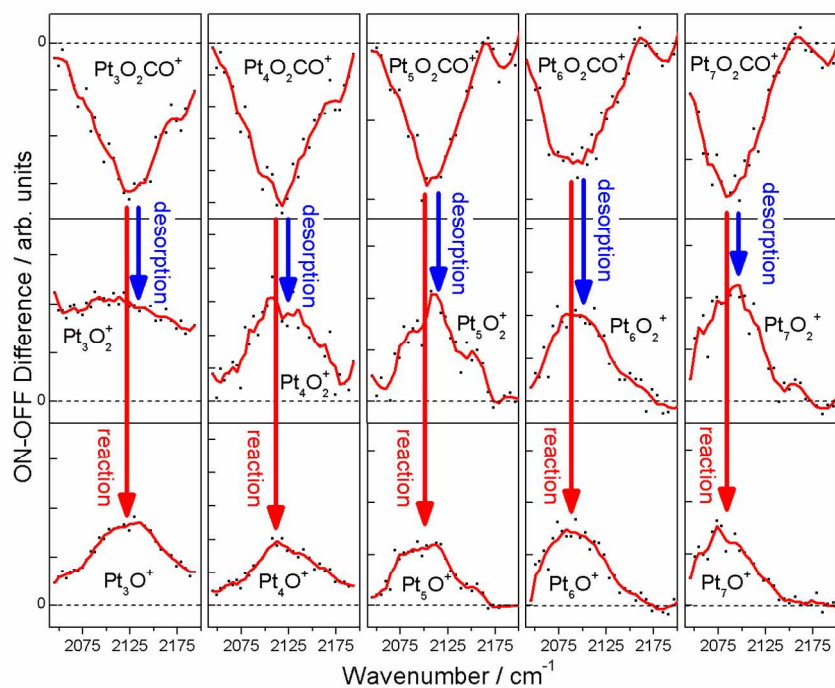


Fig. 6 Infrared driven CO oxidation $\text{Pt}_n\text{O}_2\text{CO}^+$ ($n=3-7$) following excitation in the CO stretch region around 2100 cm^{-1} (black dots: raw data, red line: 5 point adjacent average). Both CO desorption (leading to Pt_nO_2^+) and CO oxidation (generating Pt_nO^+) represent important channels across the 5 range of cluster size studied.

Table 2 Branching ratios for the CO oxidation reaction and CO loss following IR heating of $\text{Pt}_n\text{O}_2\text{CO}^+$ clusters.

n	Spectral range / cm^{-1}	% Reaction ¹	% Desorption ¹
3	2088 – 2169	43	57
4	2083 – 2153	38	62
5	2079 – 2134	40	60
6	2055 – 2134	46	54
7	2055 – 2123	38	62

¹⁰ ¹estimated uncertainty = $\pm 5\%$

4.3 Calculated reaction pathways

We have undertaken preliminary calculations in an attempt to identify a plausible mechanism for the CO oxidation reaction on the $\text{Pt}_4\text{O}_2\text{CO}^+$ cluster. For the example of the lowest energy structure, key stationary points in the pathway are shown in Figure 7. The pathways were identified by identifying likely transition states (in this case by analogy with those calculated for the same reaction on extended surfaces by Eichler³⁸) and then using the eigenvector following method³⁹ to link these with local minima.

These calculations proved considerably more challenging than similar pathways for the unimolecular decomposition of N_2O on rhodium clusters which we have studied previously. In the present case the metal atom framework is much more flexible than was the case for rhodium and the platinum atoms are more intimately involved in the reaction. Indeed, the metal atom framework itself is highly fluxional and we have identified several mechanisms involving apparent migration of Pt atoms. Furthermore, the addition of even a single additional oxygen atom to a bare Pt_n^+ cluster is enough to change its structure markedly. We calculate the CO binding energy to the lowest energy structure to be 2.71 eV which thus represents the minimum energy required to desorb the CO. This compares well with the CO binding to Pt_n^- clusters experimentally determined by Shi *et al.* to be 220-250 kJ mol^{-1} (2.3-2.6 eV) by collisional induced dissociation and the calculated ~2.6 eV binding energy on neutral Pt_4 determined by Xu *et al.*⁴⁰ The presence of oxygen adatoms, can, of course, profoundly affect the binding energies of co-adsorbates and we recently demonstrated such an effect in infrared driven reactivity.¹⁵

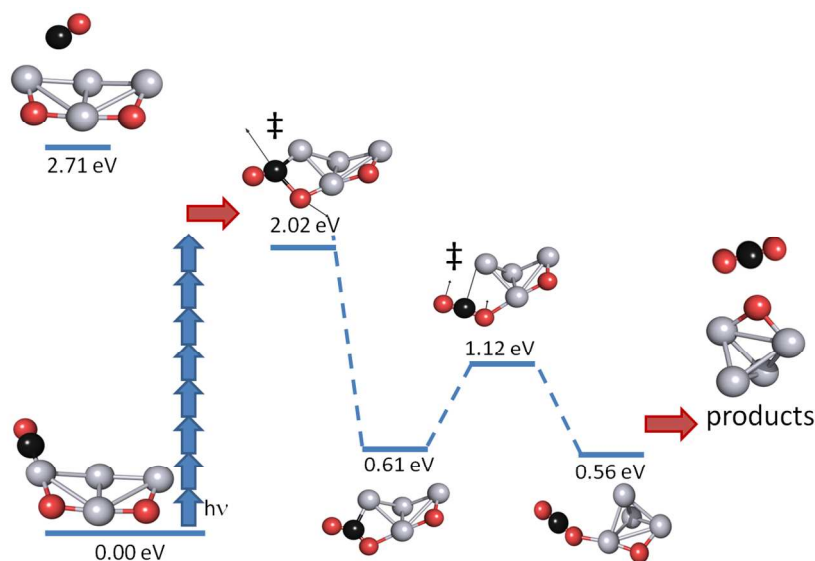


Fig 7 Key stationary points calculated on the CO oxidation reaction pathway on $\text{Pt}_4\text{O}_2\text{CO}^+$ heated by infrared multiple-photon excitation *via* the CO stretching vibration. Structures shown result from vector following from the transition states and do not necessarily represent the lowest energy structures.⁴⁰ The arrows shown represent the approximate energy of each IR photon.

The activation barrier for $\text{CO}_{(\text{ads})} + \text{O}_{(\text{ads})} \rightarrow \text{CO}_{2(\text{g})}$ on Pt(111) extended surfaces is strongly coverage-dependent⁴¹ but at low coverage has variously been determined to be from 100 kJ mol^{-1} (1 eV) by molecular beam scattering,⁴² to 166 kJ mol^{-1} (1.7 eV) by temperature programmed desorption.⁴³ In this context the reaction barrier in Figure 7 is markedly higher than might be expected. It is also significantly higher than the 0.74 eV barrier identified in the DFT study on extended Pt(111).³⁸ These reaction barriers, however, and indeed the geometries of the transition states themselves, are highly dependent on the exchange-correlation functional used in the calculations.

10

5 Summary and conclusions

Infrared multiple photon absorption spectroscopy has been applied to CO decorated platinum cluster oxides in the gas-phase. Well-resolved vibrational structure in both the Pt–O stretch and CO stretch regions permit structural assignments by comparison with DFT simulations. Additional features around 940 cm^{-1} provide evidence of higher-lying isomeric forms, possibly peroxo-structures.

In a significant extension of the technique over the unimolecular decompositions to which it has been applied to date, efficient CO oxidation has been observed following IR excitation of $\text{Pt}_n\text{O}_2\text{CO}^+$ in the region of the CO stretch. Preliminary calculations of the reaction pathway have identified plausible transition states below the CO desorption energy consistent with the experimental findings. These observations lend further support to the thermal nature of the reactivity observed and offer the prospect of studying important catalytic reactions as a function of both cluster size and isomeric structure. As we have shown previously, this cluster analogue of temperature programmed reactions is exquisitely sensitive to the relative barriers to reaction and/or desorption.

Acknowledgements

We gratefully acknowledge the support of the Stichting voor Fundamenteel Onderzoek der Materie (FOM) for providing FELIX beam time and the FELIX staff, in particular Dr. B. Redlich and Dr. A.F.G. van der Meer, for their skillful assistance. This work is supported by the Deutsche Forschungsgemeinschaft through research grant FI893/3-1. DJH thanks the Alexander-von-Humboldt-Stiftung for support. ACH and GAC are grateful to the EPSRC for support. We are grateful to the Oxford Supercomputing Centre and the EPSRC UK National Service for Computational Chemistry Software (NSCCS) at Imperial College London for the use of their computing resources in performing the computational aspects of this work.

40

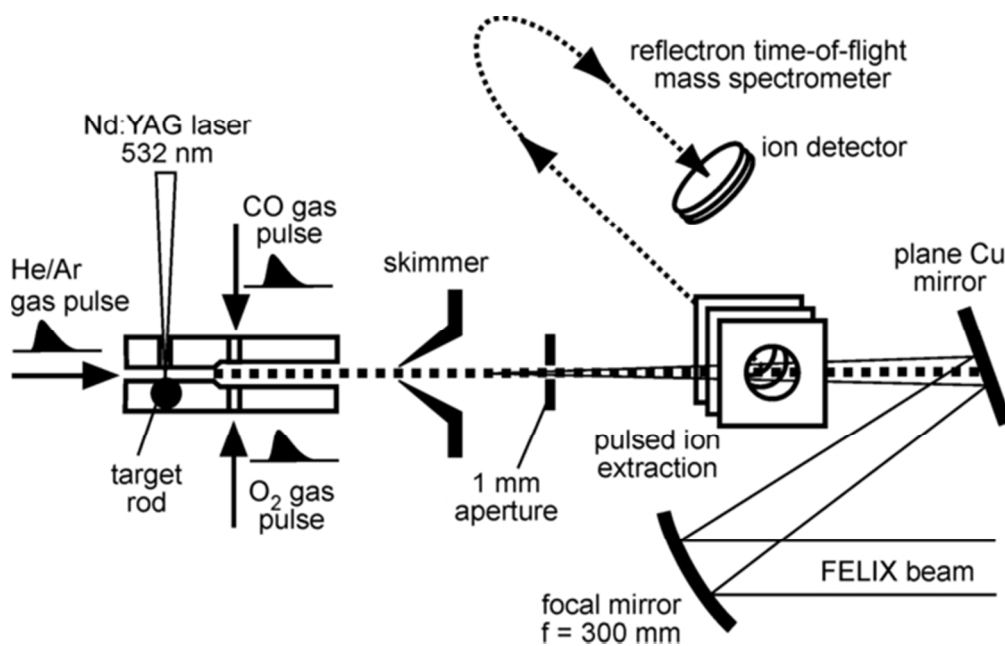
References

† Electronic Supplementary Information (ESI) available: Relative energies and structures of the calculated lowest-lying $\text{Pt}_4\text{O}_2\text{CO}^+$ structures with dissociatively adsorbed O_2 and the lowest-lying structures with O_2 in a peroxo motif. See DOI: 10.1039/b000000x/

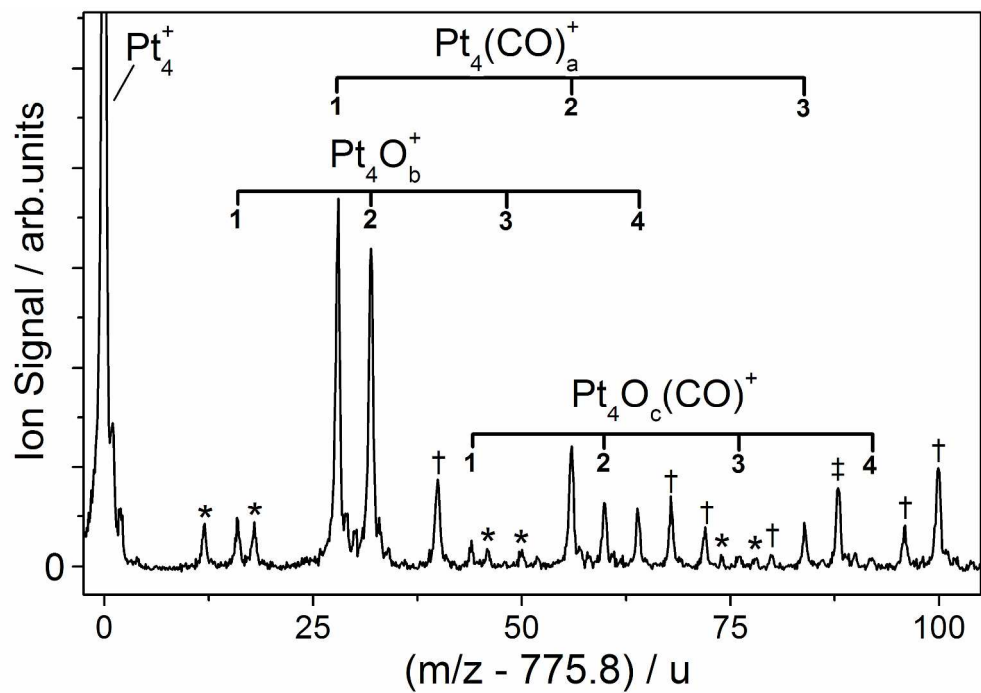
5

1. G. A. Somorjai, *Chemistry in two dimensions : surfaces*, Cornell University Press, Ithaca, 1981.
2. A. Cho, *Science*, 2003, **299**, 1684-1685.
3. P. B. Armentrout, *Annu. Rev. Phys. Chem.*, 2001, **52**, 423-461.
- 10 4. P. B. Armentrout, *Eur. J. Mass Spectrom.*, 2003, **9**, 531-538.
5. M. B. Knickelbein, *Annu. Rev. Phys. Chem.*, 1999, **50**, 79-115.
6. M. Okumura, L. I. Yeh, J. D. Myers and Y. T. Lee, *J. Chem. Phys.*, 1986, **85**, 2328-2329.
7. G. Gregoire and M. A. Duncan, *J. Chem. Phys.*, 2002, **117**, 2120-2130.
8. A. Fielicke, G. von Helden, G. Meijer, D. B. Pedersen, B. Simard and D. M. Rayner, *J. Am. Chem. Soc.*, 2005, **127**, 8416-8423.
- 15 9. P. Gruene, D. M. Rayner, B. Redlich, A. F. G. van der Meer, J. T. Lyon, G. Meijer and A. Fielicke, *Science*, 2008, **321**, 674-676.
10. A. Fielicke, G. von Helden and G. Meijer, *Eur. Phys. J. D*, 2005, **34**, 83-88.
11. D. J. Harding, T. R. Walsh, S. M. Hamilton, W. S. Hopkins, S. R. Mackenzie, P. Gruene, M. Haertelt, G. Meijer and A. Fielicke, *J. Chem. Phys.*, 2010, **132**, 011101.
- 20 12. D. J. Harding, P. Gruene, M. Haertelt, G. Meijer, A. Fielicke, S. M. Hamilton, W. S. Hopkins, S. R. Mackenzie, S. P. Neville and T. R. Walsh, *J. Chem. Phys.*, 2010, **133**, 214304.
13. S. M. Hamilton, W. S. Hopkins, D. J. Harding, T. R. Walsh, P. Gruene, M. Haertelt, A. Fielicke, G. Meijer and S. R. Mackenzie, *J. Am. Chem. Soc.*, 2010, **132**, 1448-1449.
- 25 14. S. M. Hamilton, W. S. Hopkins, D. J. Harding, T. R. Walsh, M. Haertelt, C. Kerpel, P. Gruene, G. Meijer, A. Fielicke and S. R. Mackenzie, *J. Phys. Chem. A*, 2011, **115**, 2489-2497.
15. A. C. Hermes, S. M. Hamilton, W. S. Hopldns, D. J. Harding, C. Kerpel, G. Meijer, A. Fielicke and S. R. Mackenzie, *J. Phys. Chem. Lett.*, 2011, **2**, 3053-3057.
16. D. J. Harding, C. Kerpel, G. Meijer and A. Fielicke, *Angew. Chem. Int. Ed.*, 2012, **51**, 817-819.
- 30 17. G. Ertl, *Angew. Chem. Int. Ed.*, 2008, **47**, 3524-3535.
18. T. Matsushima, *Surf. Sci.*, 1983, **127**, 403-423.
19. U. Heiz, A. Sanchez, S. Abbet and W. D. Schneider, *J. Am. Chem. Soc.*, 1999, **121**, 3214-3217.
20. Y. Shi and K. M. Ervin, *J. Chem. Phys.*, 1998, **108**, 1757-1760.
21. O. P. Balaj, I. Balteanu, T. T. J. Rossteuscher, M. K. Beyer and V. E. Bondybey, *Angew. Chem. Int. Ed.*, 2004, **43**, 6519-6522.
- 35 22. D. Oepts, A. F. G. van der Meer and P. W. van Amersfoort, *Infrared Physics & Technology*, 1995, **36**, 297-308.
23. A. Fielicke, A. Kirilyuk, C. Ratsch, J. Behler, M. Scheffler, G. von Helden and G. Meijer, *Phys. Rev. Lett.*, 2004, **93**, 023401.
- 40 24. Turbomole v6.0 2009, a development of University of Karlsruhe and Forschungszentrum Karlsruhe GmbH, 1989-2007, TURBOMOLE GmbH, since 2007; available from <http://www.turbomole.com>, (2009).
25. J. M. Tao, J. P. Perdew, V. N. Staroverov and G. E. Scuseria, *Phys. Rev. Lett.*, 2003, **91**, 146401.
- 45 26. V. N. Staroverov, G. E. Scuseria, J. M. Tao and J. P. Perdew, *J. Chem. Phys.*, 2003, **119**, 12129-12137.
27. A. Fielicke, P. Gruene, M. Haertelt, D. J. Harding and G. Meijer, *J. Phys. Chem. A*, 2010, **114**, 9755-9761.
28. D. J. Harding, C. Kerpel, D. M. Rayner and A. Fielicke, *manuscript in preparation*.
- 50 29. F. Weigend, M. Haser, H. Patzelt and R. Ahlrichs, *Chem. Phys. Lett.*, 1998, **294**, 143-152.
30. F. Weigend and R. Ahlrichs, *Phys. Chem. Chem. Phys.*, 2005, **7**, 3297-3305.
31. D. J. Wales and J. P. K. Doye, *J. Phys. Chem. A*, 1997, **101**, 5111-5116.
32. L. Xiao and L. C. Wang, *J. Phys. Chem. A*, 2004, **108**, 8605-8614.
33. Y. Ohno and T. Matsushima, *Surf. Sci.*, 1991, **241**, 47-53.
- 55 34. P. Gruene, A. Fielicke, G. Meijer and D. M. Rayner, *Phys. Chem. Chem. Phys.*, 2008, **10**, 6144-6149.
35. J. Yoshinobu and M. Kawai, *Surf. Sci.*, 1996, **363**, 105-111.
36. J. V. Nekrylova and I. Harrison, *Chem. Phys.*, 1996, **205**, 37-46.

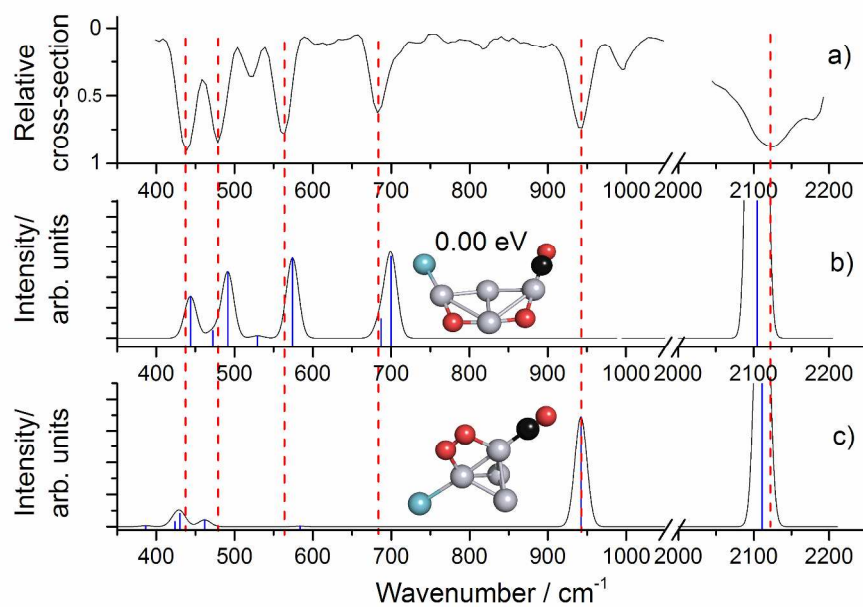
37. I. Swart, A. Fielicke, D. M. Rayner, G. Meijer, B. M. Weckhuysen and F. M. F. de Groot, *Angew. Chem. Int. Ed.*, 2007, **46**, 5317-5320.
38. A. Eichler, *Surf. Sci.*, 2002, **498**, 314-320.
39. J. Simons, P. Jorgensen, H. Taylor and J. Ozment, *J. Phys. Chem.*, 1983, **87**, 2745-2753.
- 5 40. Y. Xu, R. B. Getman, W. A. Shelton and W. F. Schneider, *Phys. Chem. Chem. Phys.*, 2008, **10**, 6009-6018.
41. J. Winterlin, S. Volkening, T. V. W. Janssens, T. Zambelli and G. Ertl, *Science*, 1997, **278**, 1931-1934.
42. C. T. Campbell, G. Ertl, H. Kuipers and J. Segner, *J. Chem. Phys.*, 1980, **73**, 5862-5873.
- 10 43. J. L. Gland and E. B. Kollin, *J. Chem. Phys.*, 1983, **78**, 963-974.



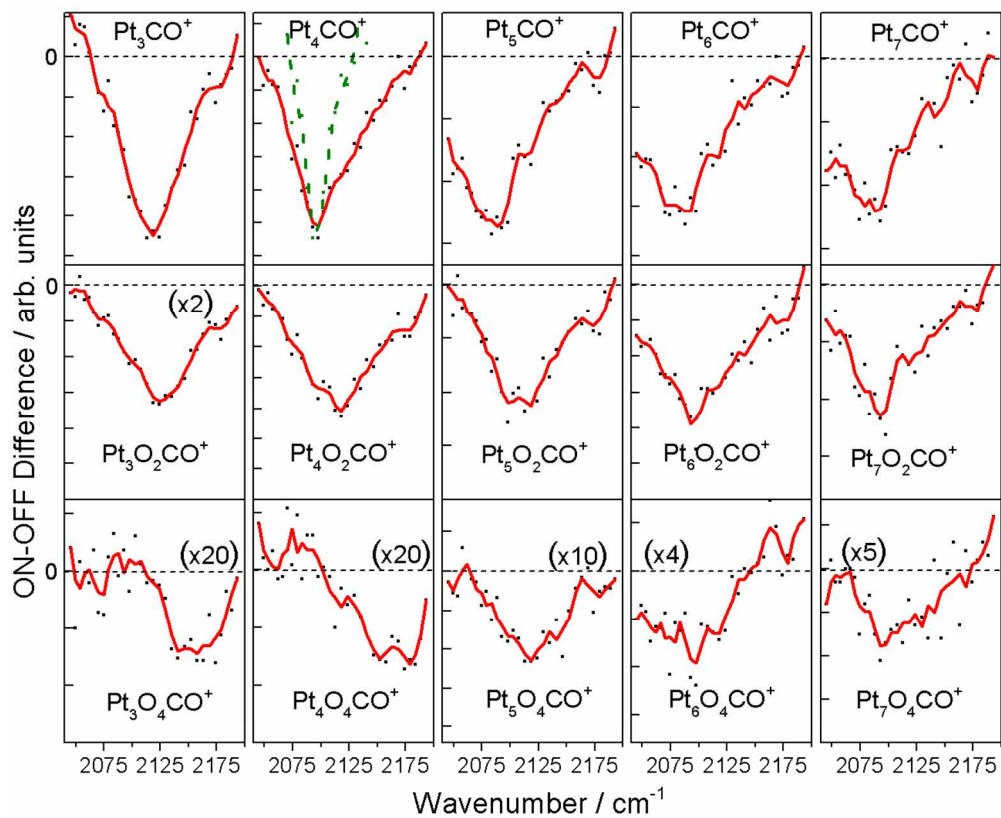
56x35mm (300 x 300 DPI)



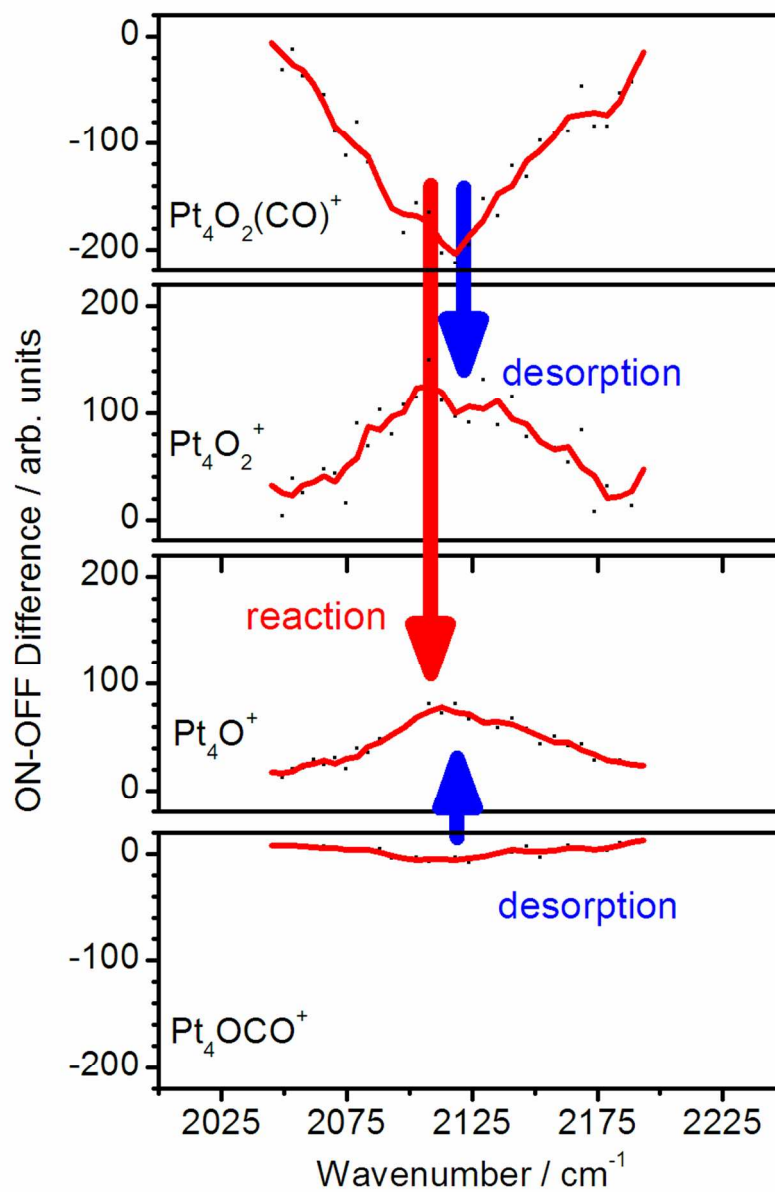
288x201mm (300 x 300 DPI)



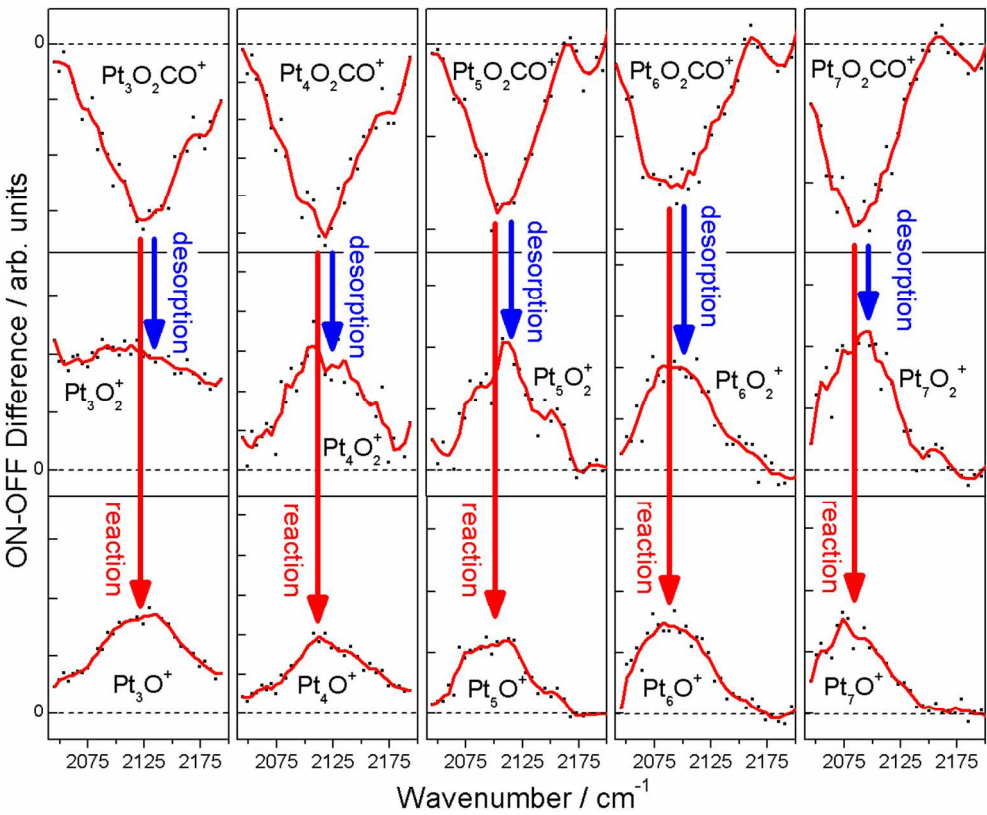
288x201mm (300 x 300 DPI)



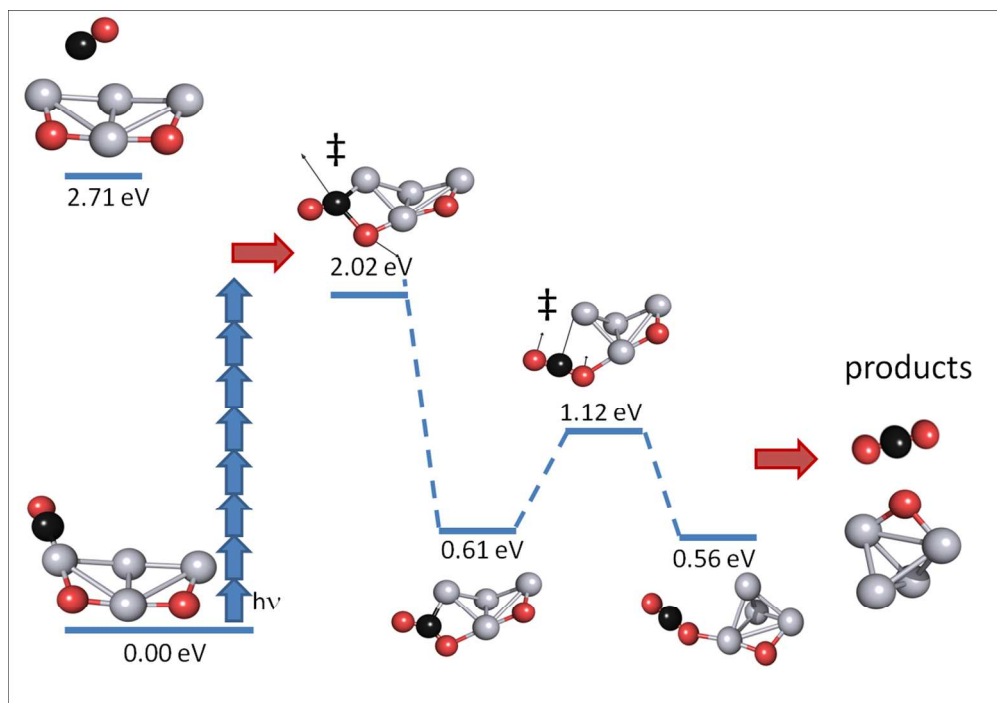
109x89mm (300 x 300 DPI)



80x119mm (300 x 300 DPI)



109x89mm (300 x 300 DPI)



233x162mm (150 x 150 DPI)

Infrared driven CO oxidation reactions on isolated platinum cluster oxides, Pt_nO_m^+

Alexander C. Hermes,^a Suzanne M. Hamilton,^a Graham A. Cooper,^a Christian Kerpel,^b Dan J. Harding,^b Gerard Meijer,^b André Fielicke^{b*} and Stuart R. Mackenzie^{a*}

^a Department of Chemistry, University of Oxford, Physical and Theoretical Chemistry Laboratory, South Parks Road, Oxford, OX1 3QZ U.K. Fax: 44 1865 275410; Tel: 44 1865 275156; E-mail: stuart.mackenzie@chem.ox.ac.uk

^b Fritz-Haber-Institut der Max-Planck-Gesellschaft, Faradayweg 4-6, D-14195 Berlin, Germany. Fax: 49 (0)30 8413 5603; Tel: 49 (0)30 8413 5622; E-mail: fielicke@fhi-berlin.mpg.de

Electronic Supplementary Information

Table S1: Structures, spin states and relative energies of the 10 lowest energy $\text{Pt}_4\text{O}_2\text{CO}^+$ structures identified based on dissociated O_2 (see Table S2 for coordinate files)

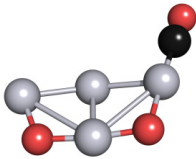
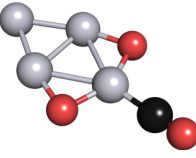
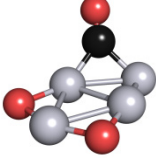
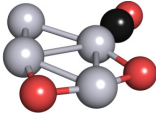
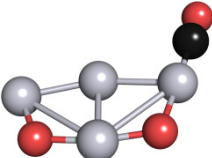

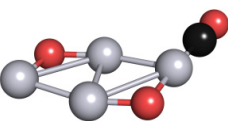
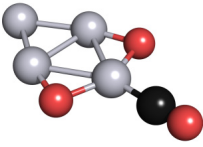
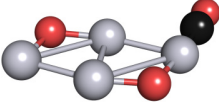
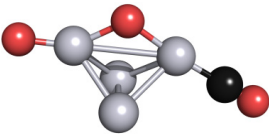
Structure Number	Structure	2S+1	Relative Energy /eV
1		2	0.00
2		2	0.07
3		2	0.11
4		2	0.11
5		4	0.22
6		2	0.23
7		2	0.27
8		4	0.31
9		4	0.33
10		2	0.37

Table S2: Coordinates for the structures in Table S1 in xyz format.

8 Structure 1 Pt 0.93061 0.77264 1.65984 Pt -1.01579 0.13788 0.28900 Pt -1.83070 2.15953 1.54907 Pt 0.90557 -0.99324 -0.93423 O 1.94870 -0.39648 0.64210 O -0.22876 1.96827 2.51765 C -0.05933 -1.62714 -2.41522 O -0.65030 -2.02145 -3.30821	8 Structure 2 Pt -3.32120 1.83109 0.21248 Pt -1.09301 1.38715 1.15561 Pt 0.57506 -0.32157 -0.02896 Pt -1.86658 0.22722 -0.95574 O 0.67479 0.78306 1.55172 O -0.45847 -0.91692 -1.54799 C 2.24596 -1.22684 -0.15207 O 3.24346 -1.76320 -0.23504
8 Structure 3 Pt -2.23744 0.20087 -0.48652 Pt -0.10740 -0.00257 0.98734 Pt 1.94638 -1.36924 -0.04649 Pt -0.09785 -0.71869 -1.54926 O 1.59378 -0.65994 1.65779 O 1.51700 -1.72407 -1.82703 C -1.26314 1.56614 0.52494 O -1.35132 2.70749 0.73923	8 Structure 4 Pt -1.36220 0.46373 -1.92198 Pt -2.10899 -0.62305 0.14425 Pt -0.40173 -0.97377 1.93070 Pt 0.48215 0.27117 -0.22219 O -2.20988 -1.49681 1.89477 O 1.28509 -0.29883 1.50132 C 1.77038 1.08909 -1.32163 O 2.54519 1.56847 -2.00524
8 Structure 5 Pt 1.56148 1.44099 -0.12240 Pt -0.06534 -0.21909 -0.89492 Pt -0.59565 -0.25683 1.56630 Pt 0.99132 0.33052 -3.06799 O 2.00837 1.48340 -1.96989 O 0.83688 1.10337 1.56755 C -1.95520 -1.54925 1.49504 O -2.78185 -2.33311 1.42632	8 Structure 6 Pt -1.09931 -0.68641 -1.10906 Pt -0.60868 0.01284 1.27910 Pt 0.88467 2.19932 1.47722 Pt 0.97236 0.72637 -0.72809 O -0.37571 1.39619 2.59182 O 1.78051 2.37021 -0.14850 C -0.88205 -2.45971 -1.56852 O -0.67180 -3.55881 -1.79397
8 Structure 7 Pt -2.06608 2.63430 1.30467 Pt 0.28092 0.89182 0.19040 Pt -2.11475 0.33179 0.36720 Pt 0.32586 -1.51961 -0.48788 O -1.60591 -1.38654 -0.21176 O -0.26305 2.61600 0.79675 C 2.16768 -1.72315 -0.85969 O 3.27534 -1.84459 -1.09968	8 Structure 7 Pt -3.32146 1.85218 0.20184 Pt -1.07646 1.39965 1.17355 Pt 0.58060 -0.32798 -0.02684 Pt -1.86686 0.21374 -0.97832 O 0.67911 0.79727 1.57522 O -0.46852 -0.92496 -1.57172 C 2.23865 -1.23416 -0.14607 O 3.23494 -1.77573 -0.22766
8 Structure 9 Pt -1.02452 0.00313 3.41340 Pt 0.50632 0.16208 0.68664 Pt -1.86832 -0.39013 1.12781 Pt -0.23891 -0.17272 -1.70792 O -1.90988 -0.53598 -0.73795 O 0.63241 0.32667 2.59570 C 1.43589 0.19184 -2.47172 O 2.46702 0.41511 -2.90595	8 Structure 10 Pt 0.65136 0.73108 2.00862 Pt -0.95029 -1.01529 1.02693 Pt -1.03600 1.38572 0.18814 Pt 0.45437 -0.35954 -1.08139 O 1.54939 0.22007 0.42309 O 0.79173 1.28930 3.64646 C -0.45592 -0.94961 -2.63800 O -1.00463 -1.30173 -3.57385

Table S3: Structures, spin states and relative energies of the 10 lowest energy $\text{Pt}_4\text{O}_2\text{CO}^+$ structures identified with peroxo motifs.

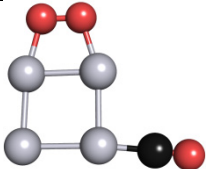
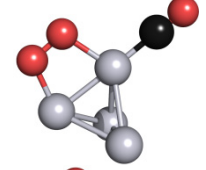
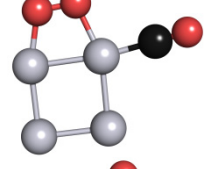
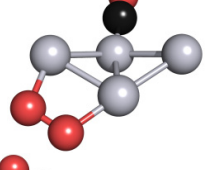
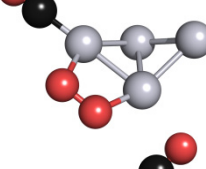
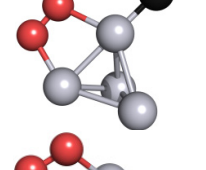
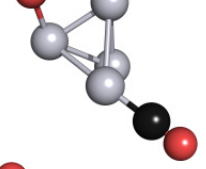
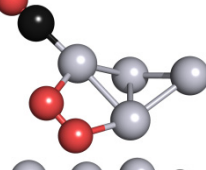
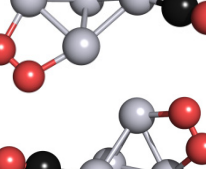
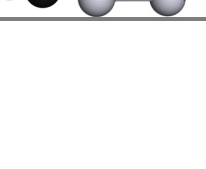
Structure Number	Structure	2S+1	Energy relative to Structure 1 /eV	Energy relative to Structure 11 /eV
11		2	1.39	0.00
12		2	1.52	0.12
13		2	1.52	0.13
14		2	1.58	0.19
15		2	1.61	0.22
16		4	1.62	0.23
17		2	1.70	0.31
18		4	1.75	0.36
19		4	1.76	0.37
20		4	1.78	0.38

Table S4: Coordinates for the structures in Table S3 in xyz format.

8 Structure 11 Pt -0.99586 -1.34073 -0.09633 Pt -0.80267 2.10125 -0.12754 Pt 0.84750 0.34284 0.11402 Pt -2.69544 0.54048 -0.33166 O 0.92543 2.98972 0.10203 O 1.83460 2.00563 0.23424 C 0.12195 -2.84850 0.02145 O 0.76451 -3.79069 0.08379	8 Structure 12 Pt -0.56007 -1.08716 1.70216 Pt 0.90939 -2.38589 -0.02117 Pt 0.12473 0.16901 -0.26805 Pt -1.49049 -1.96003 -0.56018 C 0.65039 1.19753 -1.79776 O 0.96450 1.78133 -2.72444 O -0.11514 1.52531 1.31809 O -0.48332 0.75991 2.35135
8 Structure 13 Pt -1.29037 -2.09094 0.00391 Pt -1.64996 1.33525 -0.00969 Pt 0.31683 -0.15505 0.00100 Pt -3.19684 -0.59158 -0.00434 O -0.12112 2.50551 0.00132 O 0.98798 1.75760 0.00789 C 1.97778 -1.10545 0.00276 O 2.97569 -1.65534 -0.00284	8 Structure 14 Pt 0.27152 -2.49746 -0.47773 Pt 0.54545 1.56040 -0.61504 Pt 1.67477 -0.54222 0.07373 Pt -0.90979 -0.40559 0.32530 O 2.21305 2.13355 0.14266 O 2.83569 0.99341 0.56389 C -2.75520 -0.55959 0.08782 O -3.87549 -0.68251 -0.10062
8 Structure 15 Pt -0.82750 -3.04449 -0.96201 Pt -0.17637 0.46515 0.02610 Pt 0.83036 -1.79322 0.35989 Pt -1.80797 -1.40349 0.64674 O 1.83739 0.77358 0.17990 O 2.28908 -0.45505 0.45571 C -0.86168 2.20680 -0.26279 O -1.28330 3.25072 -0.44354	8 Structure 16 Pt -0.20268 -1.15349 1.78920 Pt 0.81431 -2.48210 -0.23564 Pt 0.39391 0.13354 -0.21309 Pt -1.57080 -1.64387 -0.36028 C 0.74054 1.14070 -1.80147 O 0.95541 1.73209 -2.75170 O -0.40804 1.52081 1.27706 O -0.72266 0.75231 2.29591
8 Structure 17 Pt -1.47108 0.72236 0.93660 Pt 0.06007 -1.14181 -0.01636 Pt 0.32757 1.67741 -0.32787 Pt -1.41885 0.09479 -1.62328 C 0.93633 -2.44692 -1.03639 O 1.43750 -3.24390 -1.68250 O 0.55615 2.43546 1.50193 O -0.42769 1.90262 2.24787	8 Structure 18 Pt -0.91607 -3.00985 -0.96249 Pt -0.16172 0.42591 -0.07303 Pt 0.88485 -1.81828 0.25657 Pt -1.75285 -1.39978 0.73479 O 1.79456 0.80545 0.26170 O 2.32081 -0.40938 0.49387 C -0.87177 2.17859 -0.29095 O -1.29780 3.22734 -0.42047
8 Structure 19 Pt -0.96878 -1.48425 -0.18217 Pt -0.59251 2.09065 -0.98844 Pt 0.49233 0.45414 0.49220 Pt -2.18582 0.69165 0.37978 O 0.92176 3.07118 -0.12714 O 1.48182 2.18143 0.71421 C 0.09466 -3.03795 -0.17503 O 0.75653 -3.96685 -0.11341	8 Structure 20 Pt -0.30882 -0.65427 1.90706 Pt 1.20879 -2.07490 0.32209 Pt 1.33911 0.54218 0.64063 Pt -0.64811 -0.56933 -0.70211 C -0.65971 -0.36048 -2.58700 O -0.60503 -0.24782 -3.72062 O 0.27998 2.02281 1.72080 O -0.60621 1.34180 2.41915